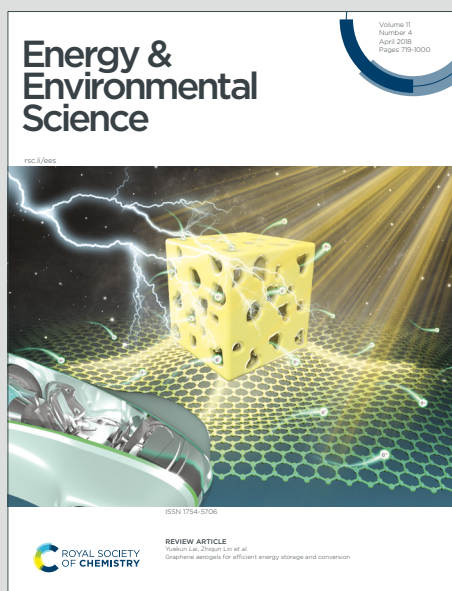


# Energy & Environmental Science

Accepted Manuscript

This article can be cited before page numbers have been issued, to do this please use: Y. Choi, D. Koo, G. Jeong, U. Kim, H. Kim, F. Huang and H. Park, *Energy Environ. Sci.*, 2022, DOI: 10.1039/D2EE00759B.



This is an Accepted Manuscript, which has been through the Royal Society of Chemistry peer review process and has been accepted for publication.

Accepted Manuscripts are published online shortly after acceptance, before technical editing, formatting and proof reading. Using this free service, authors can make their results available to the community, in citable form, before we publish the edited article. We will replace this Accepted Manuscript with the edited and formatted Advance Article as soon as it is available.

You can find more information about Accepted Manuscripts in the [Information for Authors](#).

Please note that technical editing may introduce minor changes to the text and/or graphics, which may alter content. The journal's standard [Terms & Conditions](#) and the [Ethical guidelines](#) still apply. In no event shall the Royal Society of Chemistry be held responsible for any errors or omissions in this Accepted Manuscript or any consequences arising from the use of any information it contains.

## Broader Context

Despite the remarkable performance progress of perovskite solar cells (PSCs) with power conversion efficiencies (PCEs) over 25%, mitigating the defect-originated performance degradation still remains a big challenge for further development of next-generation PSCs. Two-dimensional Ruddlesden–Popper (RP) phase perovskite is promising for passivating the defects of the bulk perovskite crystals owing to its superior environmental and structural stability. However, the charge transport efficiency of RP perovskite is highly influenced by its crystallographic orientation because of the anisotropic structural features. In this study, we introduced highly ordered vacuum-deposited butylammonium-based RP phase perovskite for developing efficient and stable inverted PSCs. By controlling the deposition rate of RP phase perovskite, which directly influenced the crystallographic orientation of RP perovskite, we successfully obtained highly ordered 2D perovskite passivation layer. The vertically orientated RP phase perovskite passivation layer applied in inverted PSCs effectively suppressed the nonradiative recombination and decomposition of underlying bulk perovskite crystals against ambient species, establishing a champion PCE of 21.4% in the resulting device with outstanding humidity and thermal stability. We expect that the perovskite interfacial engineering strategy in our study promises the development of efficient and stable PSCs with scalability.

## ARTICLE

**Vertically oriented two-dimensional Ruddlesden–Popper phase perovskite passivation layer for efficient and stable inverted perovskite solar cells**Received 00th January 20xx,  
Accepted 00th January 20xx

DOI: 10.1039/x0xx00000x

Yunseong Choi,<sup>‡a</sup> Donghwan Koo,<sup>‡a</sup> Gyujeong Jeong,<sup>a</sup> Ungsoo Kim,<sup>a</sup> Hyungmin Kim,<sup>a</sup> Fuzhi Huang,<sup>\*bc</sup> and Hyesung Park<sup>\*a</sup>

Two-dimensional Ruddlesden–Popper (RP) phase perovskite is gaining increasing attention for passivating the defects of the bulk absorber layer in perovskite solar cells (PSCs). However, owing to its anisotropic structural features, the RP perovskite orientation substantially influences the charge transport efficiency, and thereby the PSC performance. We demonstrate the use of highly oriented butylammonium RP perovskite as a surface passivation layer with bottom-up growth on the bulk perovskite absorber layer via vacuum deposition. In this process, the crystal formation time directly affects the crystallographic orientation of the passivation layer. By leveraging the passivating properties and controlled crystallinity, the RP perovskite considerably reduces the trap density of bulk perovskite and enhances the charge transport, reaching 21.4% of power conversion efficiency for vacuum-processed PSCs and improving the operational stability. The proposed passivation strategy allows to grow highly oriented RP phase perovskite passivation layers toward the development of efficient, stable, and scalable PSCs.

**Introduction**

Over the past decade, organic–inorganic lead halide hybrid perovskite with its high light absorption coefficient, low exciton binding energy, and long-range charge-carrier diffusion length has played a leading role in photovoltaic research, demonstrating impressive performance progress with perovskite solar cells (PSCs) reaching power conversion efficiencies (PCEs) above 25%.<sup>1–7</sup> Despite such rapid advances, various challenges remain to be solved to develop next-generation PSCs, especially regarding the generally poor operational stability in various environmental conditions.<sup>8,9</sup> The PSC instability primarily arises from various types of defects in perovskite (*e.g.*, surface traps, ionic vacancies, and grain boundaries), which lead to the permeation of moisture or oxygen into the perovskite layer and induce migration of perovskite constituents, thereby degrading the quality of the perovskite absorber layer.<sup>10,11</sup> To suppress defects and enhance the stability of perovskite films, various passivation strategies have been devised, such as perovskite composition engineering

and stoichiometry optimization, additive treatment, and interface engineering at the junction between the perovskite and charge transport layers.<sup>12–15</sup>

Recently, two-dimensional (2D) Ruddlesden–Popper (RP) phase perovskites have attracted research interest owing to their unique photophysical properties and superior environmental and structural stability.<sup>16</sup> Layered RP perovskites have general formula  $L_2A_{n-1}B_nX_{3n+1}$ , where L is a bulky ligand cation, A and B are monovalent organic and divalent metal cations, respectively, X is a halide anion, and n is the thickness of  $[BX_6]^{4-}$  octahedral layers.<sup>17</sup> When alternating organic and inorganic layers of 2D perovskite are deposited on a 3D organic–inorganic lead halide hybrid perovskite, the hydrophobic bulky organic spacer helps protecting the underlying bulk perovskite from decomposition and prevents chain reactions that form irreversible  $PbX_2$ , thus enhancing the device stability.<sup>18</sup> However, the lower carrier mobility and narrower absorption windows of RP perovskite impose a tradeoff between photovoltaic stability and efficiency.<sup>19</sup> To circumvent this tradeoff, complementary approaches involving the application of functionalized organic spacers and control of the RP perovskite formation are often adopted for simultaneously improving stability and efficiency in PSCs.<sup>20,21</sup> In optoelectronic applications based on 2D organic–inorganic lead halide perovskite, the crystallographic orientation is important because the inorganic  $[PbX_6]^{4-}$  octahedral layers are sandwiched by two insulating layers of organic spacers. Therein, a vertically oriented layered structure can considerably complement the interfacial charge transport from the perovskite absorber layer to the corresponding electrodes.<sup>22</sup> Various studies have been focused on orientating RP phase layered perovskite vertically by solution processes

<sup>a</sup> Department of Materials Science and Engineering, Graduate School of Semiconductor Materials and Devices Engineering, Perovtronic Research Center, Low Dimensional Carbon Materials Center, Ulsan National Institute of Science and Technology, Ulsan 44919, Republic of Korea.

<sup>b</sup> State Key Laboratory of Advanced Technology for Materials Synthesis and Processing, Wuhan University of Technology, Wuhan, 430070, PR China.

<sup>c</sup> Foshan Xianhu Laboratory of the Advanced Energy Science and Technology Guangdong Laboratory, Foshan, 528216, PR China.

<sup>†</sup> Electronic Supplementary Information (ESI) available. See DOI: 10.1039/x0xx00000x

<sup>‡</sup> These authors contributed equally to this work.

such as additive engineering and hot casting.<sup>23,24</sup> However, available solution processes typically lead to the formation of an intermediate phase and uncontrollable interphase mixing of the 2D and 3D perovskites, hindering the growth of finely oriented RP perovskite.

Apart from the solution approach, vacuum deposition technique has also been widely adopted in photovoltaic research owing to its facile processability toward forming large-area uniform and thickness-controllable thin-films and depositing conformal films over textured surfaces.<sup>25</sup> Recently, there have been growing research interests for understanding the material properties of vacuum-deposited perovskites to improve the overall device performance.<sup>26–28</sup> In particular, passivation strategies using vacuum-deposited 2D perovskite layers were proposed to increase the operational stability of PSCs, but the accompanying efficiency drop arising from the intrinsic properties of the 2D passivation layer remains a big challenge.<sup>29,30</sup>

In this work, we demonstrate highly stable and efficient PSCs using vacuum-deposited *n*-butylammonium bromide (BABr)-based 2D perovskite ((BA)<sub>2</sub>(MA)<sub>*n*-1</sub>Pb<sub>*n*</sub>I<sub>3*n*-1</sub>Br<sub>2</sub>) as the surface passivation layer on a methylammonium lead iodide (MAPbI<sub>3</sub>) photoactive layer. The proposed passivation strategy enables the controlled bottom-up growth of a vertically oriented RP perovskite layer with simple process tunability of aspects including the film deposition rate and solvent-free processability, differing from conventional solution-processed layers. We determine the direct effect of the RP perovskite deposition rate on the crystalline orientation. In addition, our solvent-free passivation layer deposition avoids the formation of unwanted intermediate phases, which cause undesirable nucleation and random orientation in RP perovskite films.<sup>31</sup> The vacuum-deposited passivation layer with highly ordered crystallinity in the out-of-plane direction eases the charge transport pathway at the interface between the perovskite and charge transport layers bypassing the insulating organic spacers, thus suppressing nonradiative recombination losses and protecting the underlying bulk perovskite layer from ambient species. The PSCs with the proposed optimized vacuum-processed passivation layer demonstrate a champion PCE of 21.4%, being the highest performance reported among PSCs based on vacuum-deposited perovskite active layer. Furthermore, the resulting PSCs provide outstanding humidity and thermal stability.

## Results and Discussion

We fabricated PSCs using MAPbI<sub>3</sub> as the photoactive layer via vacuum deposition by successive evaporation of metal halide (PbI<sub>2</sub>) and organic halide (MAI) precursors. Then, the 2D passivation layer was formed on top of the bulk perovskite using BABr-based RP perovskite ((BA)<sub>2</sub>(MA)<sub>*n*-1</sub>Pb<sub>*n*</sub>I<sub>3*n*-1</sub>Br<sub>2</sub>) through relation  $n\text{MAPbI}_3 + 2\text{BABr} = (\text{BA})_2(\text{MA})_{n-1}\text{Pb}_n\text{I}_{3n-1}\text{Br}_2 + \text{MAI}$ , which was also vacuum-deposited. For comparison, a solution-processed passivation layer was prepared alongside. The detailed fabrication process is described in the Experimental Section. A 2D RP perovskite is electrically highly

anisotropic owing to the insulating nature of constituent organic spacer layers. Consequently, manipulating the orientation of a layered RP perovskite structure becomes essential given its role as an interfacial layer. We carried out a grazing-incidence wide-angle X-ray scattering (GIWAXS) analysis to investigate the crystal orientation of three MAPbI<sub>3</sub> film configurations: 1) without passivation layer (control), 2) with solution-processed passivation layer (BABr (S)), and 3) with vacuum-processed passivation layer (BABr (V)) (Fig. 1). The scattering patterns of each perovskite film were measured with various X-ray incident angles (0.05°, 0.1°, 0.2°, and 0.5°) to elucidate the depth-dependent crystalline orientation characteristics of the perovskite. For lower incidence angles (0.05° and 0.1°), the X-ray source reveals the information near the top surface (<10 nm) of a perovskite film, and at higher angles (0.2° and 0.5°), the GIWAXS patterns can provide in-depth information of the bulk perovskite inside.<sup>32</sup> The control MAPbI<sub>3</sub> perovskite film showed continuous and uniform Debye–Scherrer diffraction rings at  $q_z = 1.0, 1.7, \text{ and } 2.0 \text{ \AA}^{-1}$  regardless of the incidence angles, corresponding to (100), (111), and (200) diffraction peaks, respectively, indicating the isotropic orientation of perovskite crystallites (Fig. 1a).<sup>5,33</sup> For the BABr (S) film, sharp diffraction peaks emerged at scattering vector  $q_z$  values of 0.32 and 0.64  $\text{\AA}^{-1}$ , which were indexed as the (020) and (040) planes of the layered RP phase perovskite crystals, respectively, with layer spacing  $d$  of approximately 20  $\text{\AA}$  ( $n = 2$ ) (Fig. 1b). Continuous Debye–Scherrer diffraction rings were still observed within a  $q_z$  range of 1.0–2.0  $\text{\AA}^{-1}$  for all incidence angles, indicating that the crystal in RP perovskite was randomly oriented. Such random orientation is typically unfavorable for vertical charge transport in solar cells and tends to degrade the overall performance.<sup>34</sup> The BABr (V) film also exhibited the (020) and (040) plane peaks along the  $z$ -axis direction, similar to the BABr (S) film (Fig. 1c). Moreover, diffraction peaks corresponding to  $n = 3$  were additionally observed at  $q_z = 0.48, 0.73, \text{ and } 1.03 \text{ \AA}^{-1}$ , which were associated with the (040), (006), and (080) planes of the RP phase perovskite, respectively (Fig. S1, ESI†). Interestingly, at lower incidence angles of 0.05° and 0.1°, sharper, stronger, and more discrete Bragg spots corresponding to the (282), (0121), and (082) planes of the RP phase perovskite were observed within a  $q_z$  range of 1.0–2.0  $\text{\AA}^{-1}$ , indicating that the RP perovskite formed from the BABr (V) film preferentially grew perpendicular to the bulk perovskite surface.<sup>22</sup> A passivation layer with such vertically oriented crystal orientation likely facilitates the interfacial charge transport in the complete solar cell. As the incidence angle increased to 0.5°, that is, further down from the top surface of the BABr (V) film, the intensity of pronounced characteristic diffraction peaks related to RP perovskite became weakened, and a Debye–Scherrer diffraction pattern corresponding to bulk MAPbI<sub>3</sub> began to dominate. This result indicates that a highly oriented RP phase perovskite thin film can be created near the surface of a 2D/3D bilayer structure.

To evaluate the atomic structural properties of the perovskite with passivation layer, we performed a high-resolution transmission electron microscopy (HRTEM) analysis on the control and perovskite films with RP phase passivation layer. As



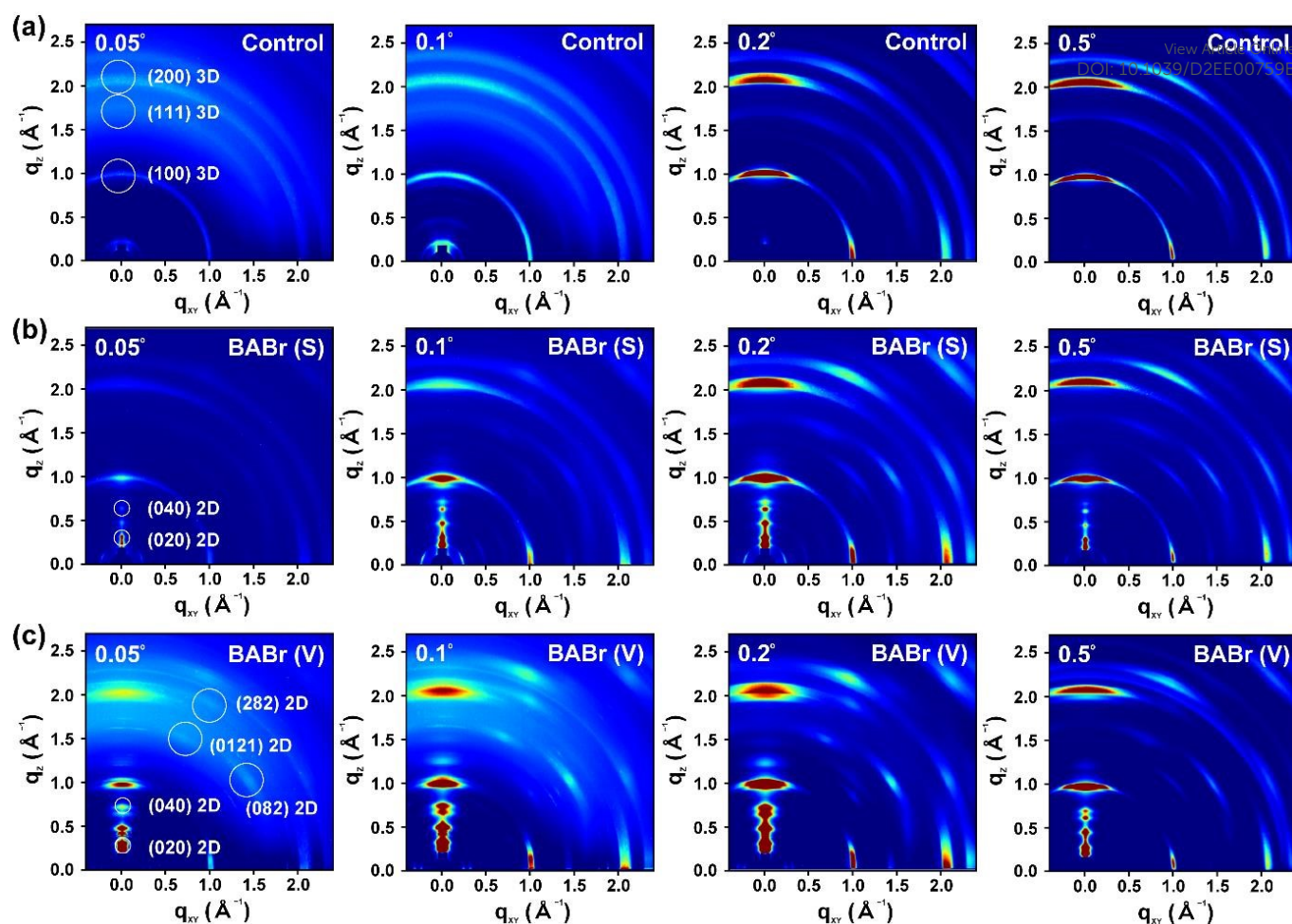


**Fig. 1** Crystallographic characterization of perovskite films with passivation layer. GIWAXS patterns of (a) control, (b) BABr (S), and (c) BABr (V) perovskite films obtained at incident angles of 0.05°, 0.1°, 0.2°, and 0.5°.

the electron diffraction difference produces phase contrast between the crystalline  $[\text{PbI}_6]^{4-}$  planes and organic cation layers, an HRTEM image can provide direct evidence of the crystal structure orientation at atomic resolution. Fig. 2a shows the uniform 3D perovskite structure formed by vacuum deposition. The BABr (S) sample showed a highly similar atomic structure to the control film but with vertically aligned RP perovskite clearly observed (Fig. 2b). Notably, substantially increased domains of the vertically aligned RP perovskite were found in the BABr (V) sample (Fig. 2c). Selected regions of the HRTEM image were further magnified and analyzed using the fast Fourier transform to examine the detailed atomic structures of perovskite. The blue circled region revealed an interplanar spacing of 3.2 Å, which suitably agreed with the (001) plane of cubic phase  $\text{MAPbI}_3$  (Fig. 2d), whereas the green and red circled regions exhibited interplanar spacings of 7.2 and 13.1 Å, corresponding to the (010) plane of RP perovskites with  $n=1$  and 2, respectively (Fig. 2e and f).<sup>35</sup> The HRTEM analysis indicates that the formation of a vertically oriented crystalline structure is more favorable for the vacuum-processed RP perovskite compared with the structure obtained from the solution process, confirming the GIWAXS results.

Nucleation and crystallization of the 2D perovskite thin film is analogous to seed-induced crystal growth, where the bulk perovskite surface serves as the seed that promotes subsequent

growth of overlying RP perovskite.<sup>36</sup> Control of the initial nucleation site becomes crucial to achieve vertical alignment, and vacuum deposition contributes to vertical crystal growth of RP phase perovskite. For liquid-phase crystal growth, thin film growth occurs simultaneously within the precursor solution. On the other hand, vapor-phase crystal growth proceeds consecutively at the exposed film surface with the gaseous RP perovskite precursor layer by layer, promoting a precise control of the deposition rate for vertically oriented perovskite crystal growth by modulating crystallization.<sup>37</sup>

We investigated the effect of the RP perovskite deposition rate on the layer crystallinity for BABr (V) films. As shown in Fig. S2a and Fig. S3a (ESI<sup>†</sup>), the slow deposition rate (0.1 Å/s) with retarded crystallization allowed the crystal growth of RP perovskite along the preferred orientation. In contrast, higher deposition rates (0.2 and 0.5 Å/s) increased the degree of randomly oriented crystal formation attributed to rapid perovskite crystallization with a limited process window, as shown in Fig. S2b and c and Fig. S3b and c (ESI<sup>†</sup>). In this situation, the characteristic spot patterns of RP phase perovskite, representing distinctive crystallographic orientations, gradually diminished with increasing deposition rates. In butylammonium-based organic-inorganic lead halide RP perovskite, the polar ( $-\text{NH}_3$ ) group is attached to the lead halide slabs and the hydrophobic alkyl groups protrude. As a result,

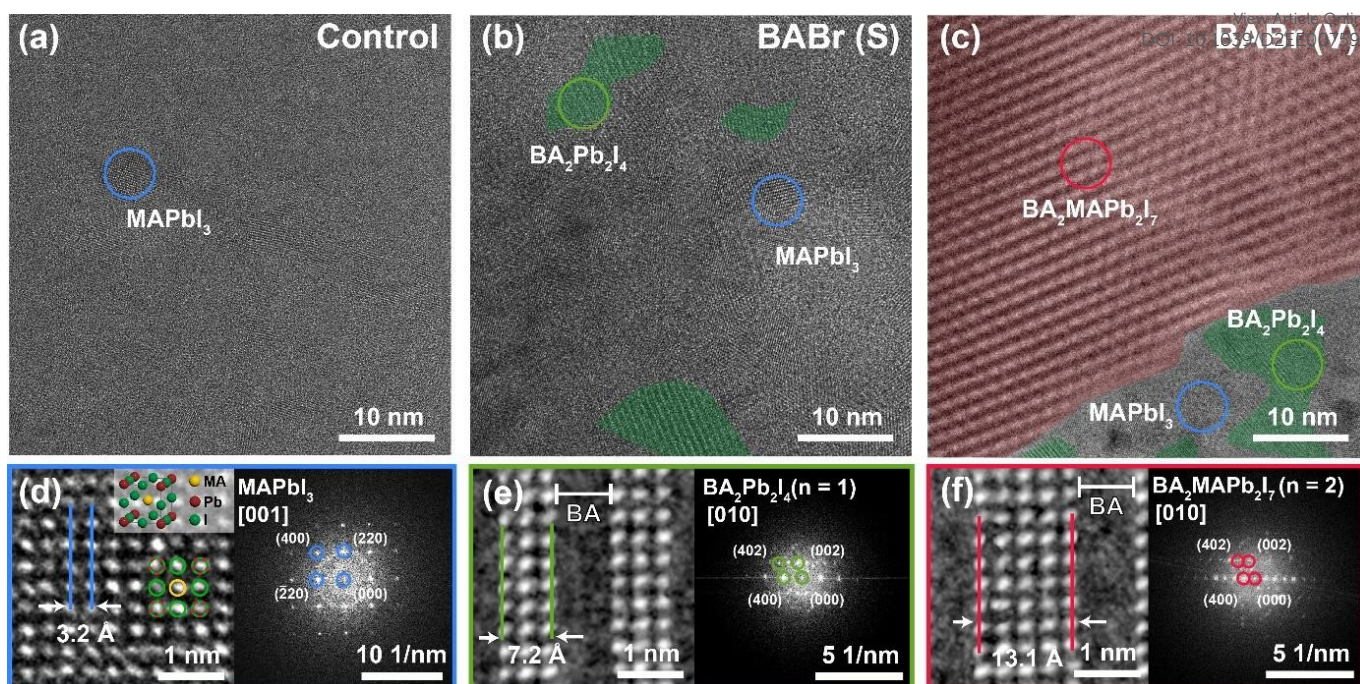


**Fig. 2** Atomic structural characterization of perovskite films with passivation layer. HRTEM images of (a) control, (b) BABr (S), and (c) BABr (V) films. Blue, green, and red circles represent MAPbI<sub>3</sub>, BA<sub>2</sub>Pb<sub>2</sub>I<sub>4</sub> (*n* = 1), and BA<sub>2</sub>MAPb<sub>2</sub>I<sub>7</sub> (*n* = 2), respectively. Magnified HRTEM images of (d) MAPbI<sub>3</sub>, (e) BA<sub>2</sub>Pb<sub>2</sub>I<sub>4</sub> (*n* = 1), and (f) BA<sub>2</sub>MAPb<sub>2</sub>I<sub>7</sub> (*n* = 2) domains with corresponding images showing the fast Fourier transform.

when RP perovskite slabs are introduced onto the bulk perovskite film, the octahedra [PbX<sub>6</sub>]<sup>4-</sup> of RP perovskite are more likely to bind with the bulk perovskite surface, while the hydrophobic long alkyl chains tend to align vertically with out-of-plane orientation.<sup>38</sup> With sufficient crystal formation time, the growth of RP perovskite with the preferred orientation can be dominant. For the solution-processed RP perovskite, a relatively rapid crystallization is more likely to induce randomly oriented RP phase perovskite crystals. In addition, the use of solvent causes undesirable nucleation within the as-deposited perovskite precursor solution, which further increases the tendency for randomly oriented perovskite crystal formation.<sup>25</sup> This phenomenon can be avoided during vacuum deposition, and crystal orientation control of the RP phase perovskite passivation layer can be achieved by optimizing vacuum deposition.

We then investigated the effect of the RP perovskite formation time in BABr (V) films on the resulting 2D/3D perovskite properties according to the deposition time (BABr (V)-*x* for deposition time of *x* min). Fig. 3a shows the X-ray diffraction (XRD) patterns of perovskite films prepared with different conditioned 2D passivation layers. The control film showed a tetragonal perovskite phase with distinctive (100) and (220) diffraction peaks centered at 14.12° and 28.44°, respectively. The magnified (100) and (220) plane-related XRD patterns clearly showed that an apparent peak shift to higher 2θ values occurred after BABr treatment owing to the decreased lattice spacing with increased BABr deposition time, indicating that the perovskite structure changed toward a cubic phase from the tetragonal phase with incorporated BABr (Fig. 3b–e). The introduction of Br<sup>-</sup> ions with a smaller ionic radius (1.96 Å) than I<sup>-</sup> ions (ionic radius of 2.2 Å) into MAPbI<sub>3</sub> perovskite decreases

the lattice parameters and results in a transition to an MAPbI<sub>3-x</sub>Br<sub>x</sub> structure.<sup>39</sup> Therefore, the observed changes in the diffraction peaks above indicate that the I<sup>-</sup> ions near the surface of bulk MAPbI<sub>3</sub> are partially substituted by Br<sup>-</sup> ions during vacuum deposition of the BABr layer.

With enough BABr treatment from the vacuum process (BABr (V)-10 and BABr (V)-20), additional diffraction peaks at 6.38° and 4.73° appeared, corresponding to the (002) plane of RP perovskite (BA)<sub>2</sub>(MA)<sub>n-1</sub>Pb<sub>n</sub>I<sub>3n+1</sub> for *n* = 1 and 2, respectively (Fig. 3f).<sup>32</sup> However, such XRD pattern of the RP perovskite was not observed for the control, BABr (V)-5, and BABr (S) films, indicating that the RP phase passivation layer in BABr (V)-5 and BABr (S) is very thin and undetectable. Similar results were observed from the optical absorption analysis (Fig. 3g). As shown in Fig. 3h, as the deposition time of RP perovskite increased, the absorption edge blue-shifted because of the increased band gap as the I<sup>-</sup> ions of the perovskite were replaced by Br<sup>-</sup> ions. The appearance of new excitonic absorption peaks at 570 and 608 nm (corresponding to *n* = 2 and 3, respectively) in BABr (V)-20 films confirmed the existence of RP perovskite species in the MAPbI<sub>3</sub> perovskite (Fig. 3i). However, the corresponding absorption peak was not observed from other conditioned samples, implying the formation of a thin RP perovskite film under a limited reaction time.<sup>29</sup>

We then evaluated the effect of a vertically aligned vacuum-processed perovskite passivation layer on the photovoltaic performance by fabricating p–i–n structured PSCs [ITO/poly[bis(4-phenyl)(2,4,6-trimethylphenyl)amine (PTAA)/MAPbI<sub>3</sub>/passivation layer/[6,6]-Phenyl-C<sub>61</sub>-butyric acid methyl ester (PC<sub>61</sub>BM)/ZnO/Ag] (Fig. 4a). The optimal deposition condition for the RP phase perovskite passivation



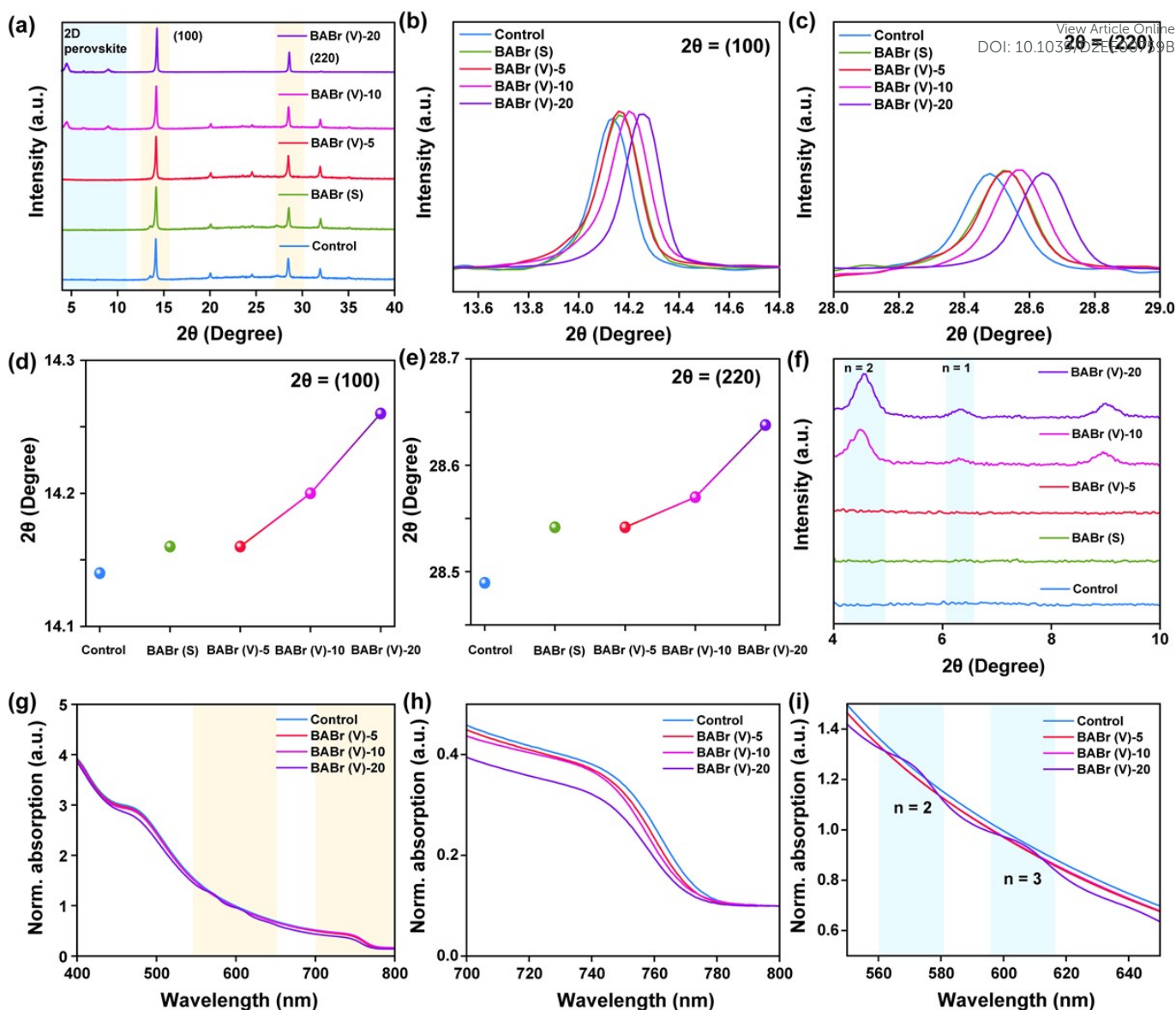


**Fig. 3** Crystalline and optical characteristics of perovskite films with different BABr treatment processes. (a) XRD patterns of control, BABr (S), and BABr (V) films with BABr deposition times of 5, 10, and 20 min. Magnified XRD patterns in (b)  $2\theta = 13.5^\circ\text{--}14.8^\circ$  and (c)  $2\theta = 28.0^\circ\text{--}29.0^\circ$  regions related to  $2\theta = (100)$  and  $(220)$  planes, respectively. Characteristic peak positions of XRD spectra corresponding to (d)  $(100)$  and (e)  $(220)$  planes. (f) XRD patterns of RP phase perovskite fingerprint from (a). (g) Ultraviolet–vis absorption spectra and magnified absorption spectra in (h) band edge region (700–800 nm) and (i) excitonic absorption peak region (550–650 nm).

layer was first determined. As shown in Fig. S4 and Table S1 (ESI<sup>†</sup>), increasing the deposition time reduced the device performance owing to the formation of a thicker RP perovskite film, as indicated by the pronouncedly reduced short-circuit current density ( $J_{SC}$ ) and fill factor (FF). The highest photovoltaic efficiency was obtained from the BABr (V)-5 film, which corresponds to the vacuum-processed BABr-based passivation layer adopted throughout this study. The current density–voltage ( $J$ – $V$ ) curves of the champion devices are shown in Fig. 4b, and the corresponding photovoltaic parameters are summarized in Table 1. The control device showed a PCE of 18.5% with a  $J_{SC}$  of  $22.7\text{ mA cm}^{-2}$ , an open-circuit voltage ( $V_{OC}$ ) of 1.07 V, and an FF of 0.76. For the solution-processed passivation layer (BABr (S) PSCs), the device performance improved with a PCE of 20.3%. For the vacuum-deposited passivation layer (BABr (V) PSCs), all the key photovoltaic parameters further

enhanced, particularly the  $V_{OC}$ , yielding a PCE of 21.4% and the highest performance among available vacuum-processed PSCs (Fig. S5 and Table S2, ESI<sup>†</sup>). Such overall improvement in the PSC performance is attributed to the enhanced charge transport from the vertically aligned interfacial passivation layer. The lower performance obtained from BABr (S) compared with BABr (V) is attributed to the randomly oriented passivation layer that can interrupt the charge transport pathway to the electrode. The external quantum efficiency of PSCs with and without passivation layer are shown in Fig. 4c. The spectrum edge of external quantum efficiency was slightly blue-shifted with the incorporation of the passivation layer owing to the increased band gap by  $\text{Br}^-$  ions replacing  $\text{I}^-$  ions. Nonetheless, an enhanced photoresponse in the overall wavelength range was observed for PSCs with passivation layer owing to the enhanced charge transport. The statistics of device

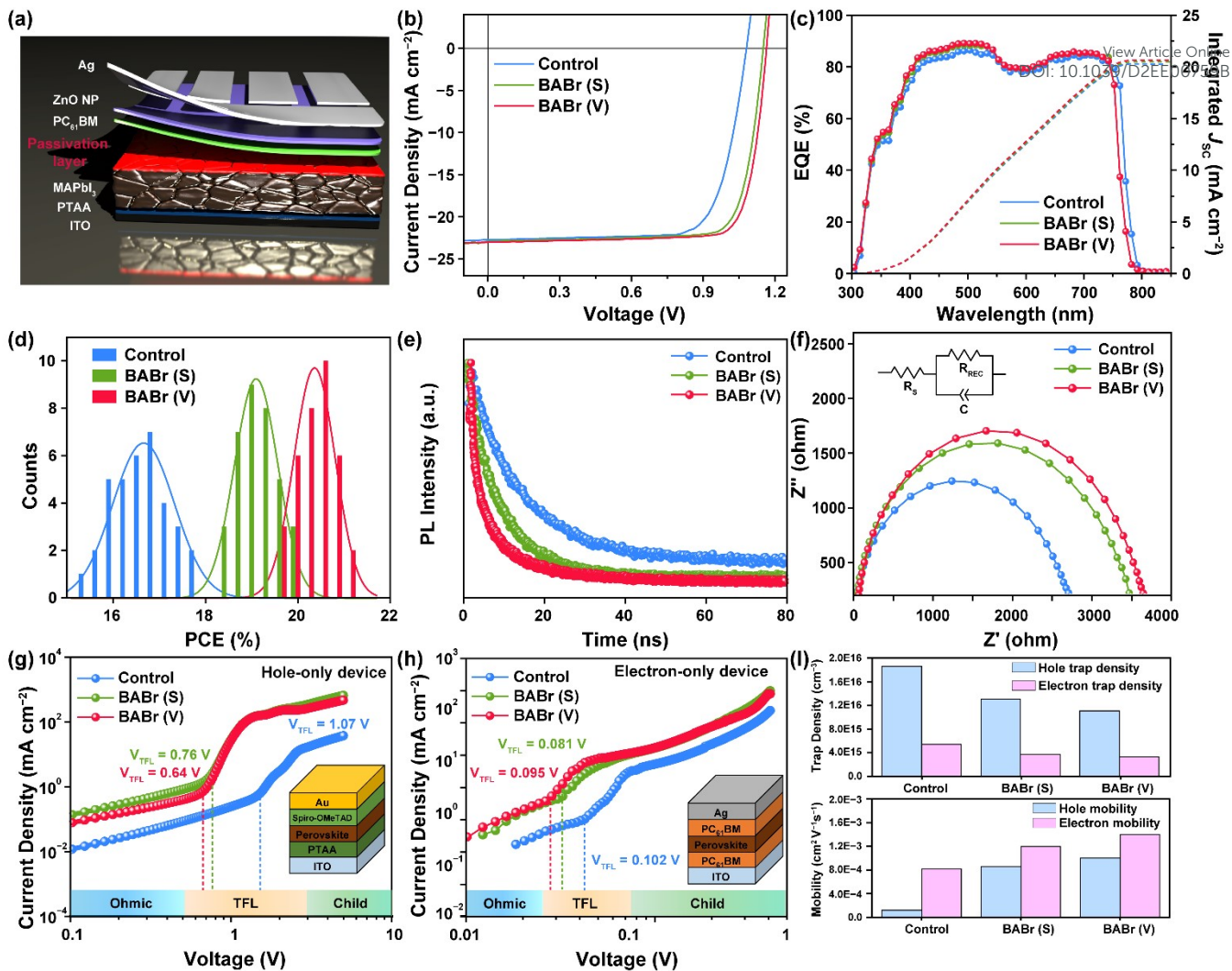


**Fig. 4** Photovoltaic performance and optoelectronic properties of PSCs. (a) Schematic of inverted PSCs. (b) J–V characteristics of optimized PSCs with passivation layer. (c) External quantum efficiency (EQE) spectra and corresponding integrated  $J_{sc}$  of PSCs with passivation layer. (d) PCE distributions of PSCs. (e) TRPL spectra measured from perovskite films with passivation layer. (f) Electrochemical impedance spectroscopy results of PSCs and corresponding equivalent circuit model (inset). J–V characteristics of (g) hole- and (h) electron-only devices with passivation layer. (i) Calculated trap density and carrier mobility values from (g) and (h).

performance were also examined by fabricating 30 individual devices per PSC type, and it was found that BABr (V) PSCs outperformed both the control and BABr (S) PSCs (Fig. 4d). Related schematic of the perovskite crystal structure and charge transport pathway for each sample is shown in Scheme 1.

To elucidate the origin of different performance characteristics, the charge-carrier dynamics of each PSC configuration was examined. The time-resolved photoluminescence (TRPL) spectroscopy measurements were carried out to investigate the charge dissociation and recombination processes between the perovskite

and charge transport layers (Fig. 4e). In TRPL analysis, the fast and slow decay processes are attributed to the photogenerated carrier quenching from the photoactive layer to the charge transport layer and bimolecular recombination in the photoactive layer, respectively.<sup>40</sup> The BABr (V) shows a large fraction of fast decay and reduced fast and slow decay lifetimes compared with BABr (S) and control, indicating more efficient charge carrier dissociation and suppressed recombination (Table S3, ESI<sup>†</sup>).

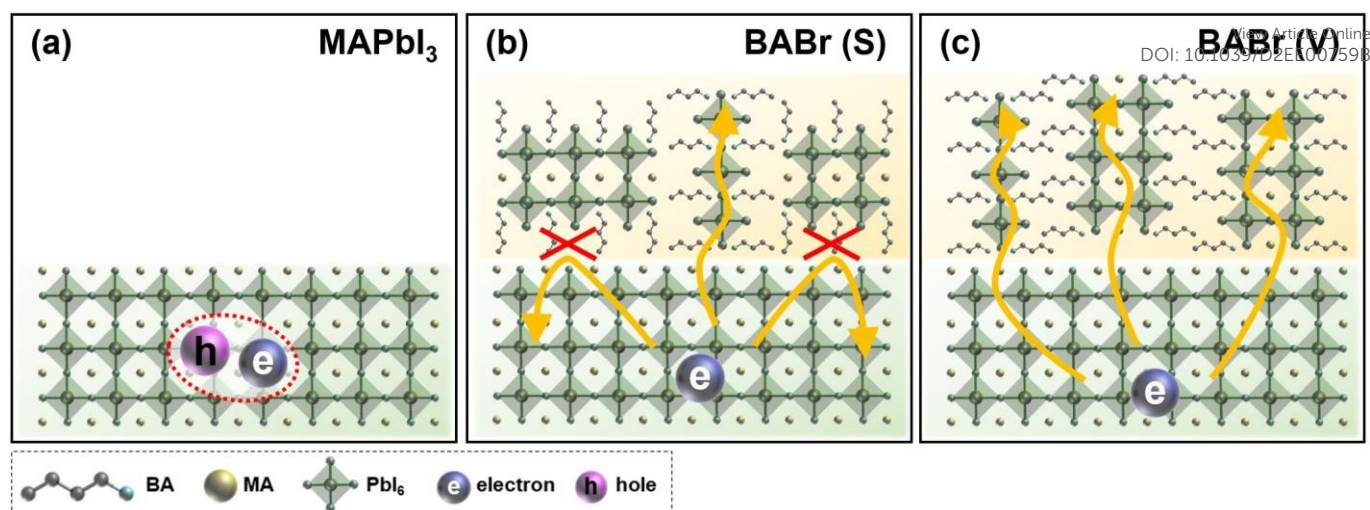
In addition, steady-state photoluminescence analysis was carried out with the perovskite films without charge transport layers. As shown in Fig. S6 (ESI<sup>†</sup>), the steady-state

**Table 1** Photovoltaic parameters of PSCs with passivation layer obtained along reverse scan direction.

Perovskite	$J_{sc}$ [mA cm <sup>-2</sup> ]	$V_{oc}$ [V]	FF	PCE [%]	Integrated $J_{sc}$ [mA cm <sup>-2</sup> ]
Control	22.7 (20.3 ± 2.5) <sup>a)</sup>	1.07 (1.04 ± 0.05)	0.76 (0.72 ± 0.08)	18.5 (17.7 ± 2.0)	21.0
BABr (S)	22.9 (20.7 ± 2.4)	1.14 (1.10 ± 0.04)	0.78 (0.73 ± 0.07)	20.3 (18.5 ± 1.8)	21.2
BABr (V)	23.0 (21.0 ± 2.2)	1.16 (1.12 ± 0.04)	0.80 (0.75 ± 0.07)	21.4 (20.2 ± 1.5)	21.5

<sup>a)</sup> The average values are obtained from 30 devices with the standard deviations.





**Scheme 1** Schematic of perovskite crystal structure and charge transport for (a) control, (b) BABr (S), and (c) BABr (V) films.

photoluminescence intensity was considerably enhanced for the BABr (V) film compared with the control and BABr (S) films, which indicated suppressing nonradiative recombination in perovskite film by reducing the perovskite surface defects with vacuum-processed RP phase passivation layer. Moreover, the peak of the photoluminescence spectrum shifted to a higher energy with the deposition of the RP perovskite passivation layer owing to an increased bandgap, confirming the findings from the optical absorption analysis.

To study the effect of the RP perovskite passivation layer on charge transfer of PSCs, electrochemical impedance spectroscopy was applied. As shown in Fig. 4f, an increased recombination resistance ( $R_{\text{rec}}$ ), obtained by fitting the equivalent circuit model, was observed for the BABr (V) PSC compared with the BABr (S) and control PSCs, indicating that charge-carrier recombination in the BABr (V) PSC can be suppressed via enhanced carrier transport and reduced trap sites. In addition, the improved current signal for BABr (V) analyzed by conductive atomic force microscope (AFM) further verified the suppressed carrier recombination and enhanced carrier transport by BABr (V) (Fig. S7, ESI†).<sup>41</sup> The light-intensity-dependent characteristics of  $V_{\text{OC}}$  and  $J_{\text{SC}}$  were also examined to determine the photogenerated charge recombination dynamics. As shown in Fig. S8a (ESI†), the  $V_{\text{OC}}$  values of all samples exhibited linear dependency over the considered light-intensity range. In addition, the ideality factor ( $n$ ) extracted from the linear fitting of  $V_{\text{OC}} \propto \frac{nkT}{q} \ln(I)$ , where  $k$  is the Boltzmann constant,  $T$  is the absolute temperature, and  $q$  is the elementary charge, was the smallest for the BABr (V) PSC, verifying that trap-assisted recombination losses are almost suppressed by using the vacuum-processed passivation layer. For the light-intensity-dependent  $J_{\text{SC}}$  relation, a typical power law dependence was obtained,  $J_{\text{SC}} \propto I^\alpha$ , where  $I$  is the light intensity, and the fit slopes ( $\alpha$ ) were 0.97, 0.99, and 0.99 for the control, BABr (S), and BABr (V) PSCs, respectively (Fig. S8b, ESI†), demonstrating that bimolecular recombination is suppressed in BABr-based PSCs.

To further explore the charge-carrier dynamics in the bulk perovskite films with passivation layer, the trap density and

mobility characteristics were analyzed using the space-charge limited current method. Fig. 4g and h show the dark  $J$ - $V$  curves of hole- and electron-only devices with structures of ITO/PTAA/perovskite/2,2',7,7'-Tetrakis[N,N-di(4-methoxyphenyl)amino]-9,9'-spirobifluorene (Spiro-OMeTAD)/Au and ITO/PC<sub>61</sub>BM/perovskite/PC<sub>61</sub>BM/Ag, respectively. The trap density ( $N_t$ ) was calculated by the trap-filled limit voltage ( $V_{\text{TFL}}$ ) as  $N_t = \frac{2\varepsilon_0\varepsilon_r V_{\text{TFL}}^2}{eL^2}$ , where  $\varepsilon_0$  and  $\varepsilon_r$  are the vacuum and relative dielectric constants of MAPbI<sub>3</sub> ( $\varepsilon_r = 25$ ), respectively,  $e$  is the elementary charge, and  $L$  is the thickness of the perovskite film. The carrier mobility values were calculated from the Mott-Gurney law as  $J = \frac{9}{8} \varepsilon_r \varepsilon_0 \mu \frac{V^2}{d^3}$ , where  $\varepsilon_r$  is the relative permittivity of the sample,  $\varepsilon_0$  is the dielectric permittivity,  $\mu$  is the hole mobility, and  $d$  is the sample thickness. As shown in Fig. 4i and Table S4 (ESI†), the calculated hole ( $N_{\text{th}}$ )/electron trap densities ( $N_{\text{te}}$ ) were  $1.86 \times 10^{16}/5.44 \times 10^{15}$ ,  $1.31 \times 10^{16}/3.74 \times 10^{15}$ , and  $1.11 \times 10^{16}/3.33 \times 10^{15} \text{ cm}^{-3}$  for the control, BABr (S), and BABr (V) films, respectively. A similar trend was found for the hole ( $\mu_h$ ) and electron mobility ( $\mu_e$ ) values. The lower hole and electron trap state density in the passivated perovskite film along with the enhanced and balanced mobility were the primary contributors to the reduced charge recombination loss and facilitated charge transport. In addition, the morphological features of perovskite films with passivation layer were investigated through the AFM and scanning electron microscope (SEM). Since the thickness of the optimized RP perovskite passivation layer is very thin, dramatic morphological changes were not observed within each condition. However, as shown in Fig. S9, the root mean square (RMS) roughness values of control and BABr (V) were found to be similar, whereas BABr (S) had slightly lower RMS value. Further, the edges of the bulk perovskite grains in BABr (S) exhibited rather blunted features (Fig. S10). Such morphological differences seem to originate from the different nature of the deposition method; the vacuum deposition process can provide more conformal thin-film formation over the perovskite grains (*i.e.*, over the textured surfaces),<sup>42</sup> which is somewhat more challenging for the solution process. The suppressed

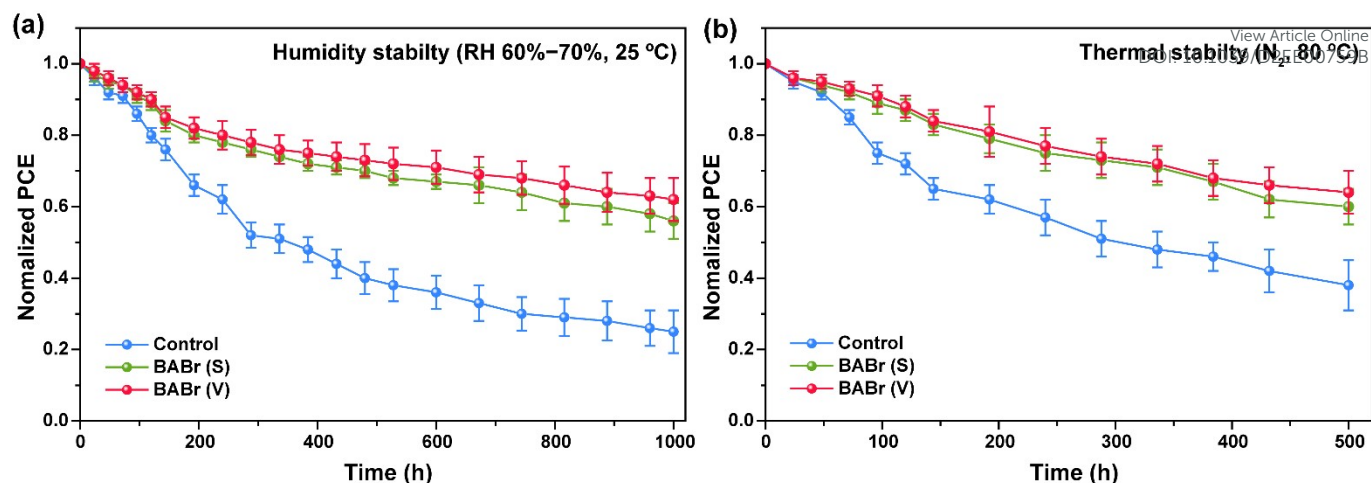


**Fig. 5** Stability analysis of PSCs with passivation layer. (a) Long-term stability against humid conditions (60%–70% relative humidity, temperature of 25 °C). (b) Thermal stability under 80 °C and inert condition (N<sub>2</sub> glovebox). The device stability was measured without encapsulations.

nonradiative recombination loss in the PSC achieved the highest efficiency in the vacuum-processed 2D/3D integrated perovskite structure.

The organic spacers in the RP phase perovskite passivation layer can prevent the penetration of moisture through the bulk perovskite layer. Therefore, RP perovskite-based PSCs likely exhibit enhanced durability during operation in external environments. Fig. 5a shows the results from a humidity stability test on the BABr-based PSC conducted under 60%–70% relative humidity at room temperature. The unencapsulated BABr (V) PSC maintained 62% of its initial PCE (average) after 1,000 h, whereas the control and BABr (S) PSCs maintained 25% and 56% of their initial performance, respectively. In addition, the larger organic spacers in the RP phase perovskite can increase the ion migration potential barrier and suppress the volatilization/escape of MA and iodine from the bulk perovskite crystal, which reduces the formation of MA and iodine vacancies, thereby improving the durability against thermal stresses.<sup>43,44</sup> The thermal stability test was conducted at 80 °C in an N<sub>2</sub> atmosphere without device encapsulation (Fig. 5b). The BABr (V) PSC exhibited the highest thermal stability, maintaining 64% of its initial performance after 500 h. Overall, the vacuum-processed passivation layer provided higher operational stability than the solution-processed device likely due to the more uniform and compact film formation of RP perovskite. These results confirm that the RP phase perovskite passivation layer mitigates both the diffusion of moisture infiltration and the migration of volatile cations and halides by surface defect passivation of the bulk perovskite, and such effect is more pronounced for PSCs with a vacuum-deposited passivation layer, possibly leading to enhanced long-term operational stability.

## Conclusions

We demonstrated highly efficient and stable PSCs with a vacuum-processed RP phase perovskite passivation layer. A highly ordered RP perovskite layer in the out-of-plane direction was obtained using vacuum deposition, which enabled the

controllable crystallization and prevented the formation of the unwanted intermediate phase. The 2D perovskite layer passivated the bulk perovskite defects and promoted the charge transport efficiency in the PSC. As a result, the BABr (V) inverted PSC enhanced the device performance with a PCE of 21.4% and high humidity/thermal stability. The analysis results provide a new perspective toward further improving the performance of PSCs by mitigating nonradiative recombination pathways in perovskites.

## Experimental Section

### Materials

The following materials were used for the PSC fabrication: PTAA (99%), PC<sub>61</sub>BM (>99.9%), MAI (>99%), PbI<sub>2</sub> (>98%), BABr (>99%), and ZnO nanoparticles (N-10) purchased from Sigma-Aldrich, Lumtec, GreatCell Solar, Tokyo Chemical Industry, 1-Material, and Avantama, respectively.

### Fabrication

The p–i–n-structured PSCs were fabricated with a configuration of ITO/PTAA/MAPbI<sub>3</sub>/passivation layer/PC<sub>61</sub>BM/ZnO nanoparticles/Ag. The ITO-coated glass substrate was cleaned with detergent, deionized water, acetone, and isopropanol. All substrates were treated with O<sub>2</sub> plasma. The PTAA (2 mg mL<sup>-1</sup> in chlorobenzene) was deposited on the ITO substrate by spin-coating at 4,000 rpm for 60 s. Then, the 300 nm thick MAPbI<sub>3</sub> perovskite film was sequentially vacuum-deposited by successively evaporating PbI<sub>2</sub> and MAI. The BABr-based perovskite passivation layer was deposited in two ways: 1) for solution process, the BABr solution (5 mg mL<sup>-1</sup> in isopropanol) was deposited by dynamic spin-coating at 4,000 rpm for 60 s; 2) for vacuum deposition, the BABr was thermally evaporated under high vacuum with a base pressure of 2 × 10<sup>-6</sup> Torr. For the electron transport layer, PC<sub>61</sub>BM (20 mg mL<sup>-1</sup> in chlorobenzene) and ZnO nanoparticles (dissolved in isopropyl alcohol) were sequentially deposited on the perovskite layer by spin-coating at 4,000 rpm for 60 s followed by annealing at 100 °C for 5 min. Finally, an Ag electrode (100 nm) was thermally evaporated.

## Measurements and Characterization

The GIWAXS measurements were conducted at the PLS-II 6D and 9A U-SAXS beamlines in the Pohang Accelerator Laboratory (South Korea). The X-rays emitted from the in-vacuum undulator were monochromated at 11.05 keV (wavelength of 1.12199 Å). At the selected incidence angles (0.05°–0.5°), the X-ray scattering was recorded by a 2D charge-coupled device detector. The XRD patterns of the MAPbI<sub>3</sub> with passivation layer were characterized using an X-ray diffractometer (Smart Lab, Rigaku). The ultraviolet–visible absorption spectra of BABr treated perovskite films were recorded using a spectrophotometer (Cary 5000, Agilent), and the steady-state photoluminescence and TRPL dynamics were measured using a fluorometer (alpha300R, WiTec photoluminescence setup) and a fluorescence lifetime spectrometer (Fluo Time 300, PicoQuant FmbH), respectively. The *J*–*V* curves were measured using a Xenon lamp solar simulator with a Keithley 2635A source meter under standard test conditions (AM 1.5G, 100 mW cm<sup>–2</sup>) with calibration using a standard silicon solar cell. The external quantum efficiency measurements were performed under ambient air conditions using an Oriel IQE 200B system. The electrochemical impedance spectra were measured using an impedance analyzer (SI1260, Solartron). The TEM image was obtained using a FEI Titan G2 60–300 system. To prepare the TEM sample, BABr treatment was conducted on 50 nm of sequentially deposited MAPbI<sub>3</sub> perovskite film on the TEM grid. The surface morphology of BABr treated perovskite films was analyzed by a cold FE-SEM micro- scope (S-4800, Hitachi) and the tapping mode AFM (MultiMode V, Veeco).

## Author Contributions

Y.C. and D.K. contributed equally to this work. Y.C. and H.P. designed the project. Y.C. and H.K. fabricated and characterized the perovskite solar cells. Y.C., G.J., and U.K. characterized the perovskite film. Y.C., D.K., and H.P. wrote the manuscript. F.H. contributed to the editing of the manuscript. H.P. supervised the project.

## Conflicts of interest

There are no conflicts to declare.

## Acknowledgements

This work was supported by the Basic Science Research Program through the National Research Foundation of Korea (NRF), funded by the Ministry of Science, ICT, and Future Planning (grant nos. 2019R1A2C1009025, 2022R1A4A2000823, 2019K1A3A1A61091347, 2021M3H4A1A02051234, and 2019M1A2A2072416).

## References

- M. A. Green, A. Ho-Baillie, H. J. Snaith, *Nat. Photonics* **2014**, *8*, 506–514.
- A. Kojima, K. Teshima, Y. Shirai, T. Miyasaka, *J. Am. Chem. Soc.* **2009**, *131*, 6050–6051. DOI: 10.1039/D2EE00759B
- NREL Best Research-Cell Efficiency Chart, <https://www.nrel.gov/pv/cell-efficiency.html> (accessed: December 2021).
- H. J. Snaith, *J. Phys. Chem. Lett.* **2013**, *4*, 3623–3630.
- D. H. Cao, C. C. Stoumpos, O. K. Farha, J. T. Hupp, M. G. Kanatzidis, *J. Am. Chem. Soc.* **2015**, *137*, 7843–7850.
- G.-W. Kim, G. Kang, M. M. Byrannvand, G.-Y. Lee, T. Park, *ACS Appl. Mater. Interfaces* **2017**, *9*, 27720–27726.
- J. H. Noh, H. I. Sang, H. H. Jin, T. N. Mandal, S. I. Seok, *Nano Lett.* **2013**, *13*, 1764–1769.
- D. Wang, M. Wright, N. K. Elumalai, A. Uddin, *Sol. Energy Mater. Sol. Cells* **2016**, *147*, 255–275.
- T. Leijtens, G. E. Eperon, N. K. Noel, S. N. Habisreutinger, A. Petrozza, H. J. Snaith, *Adv. Energy Mater.* **2015**, *5*, 1500963.
- J. Wang, W. Fu, S. Jariwala, I. Sinha, A. K.-Y. Jen, D. S. Ginger, *ACS Energy Lett.* **2019**, *4*, 222–227.
- J. M. Ball, A. Petrozza, *Nat. Energy* **2016**, *1*, 16149.
- E. Aydin, M. Bastiani, S. Wolf, *Adv. Mater.* **2019**, *31*, 1900428.
- L. Wang, C. McCleese, A. Kovalsky, Y. Zhao, C. Burda, *J. Am. Chem. Soc.* **2014**, *136*, 12205–12208.
- W. Qiu, T. Merckx, M. Jaysankar, C. Masse de la Huerta, L. Rakocevic, W. Zhang, U. W. Paetzold, R. Gehlhaar, L. Froyen, J. Poortmans, et al. *Energy Environ. Sci.* **2016**, *9*, 484–489.
- P.-W. Liang, C.-C. Chueh, S. T. Williams, A. K.-Y. Jen, *Adv. Energy Mater.* **2015**, *5*, 201402321.
- B. Kim, S. I. Seok, *Energy Environ. Sci.* **2020**, *13*, 805–820.
- B. Saparov, D. B. Mitzi, *Chem. Rev.* **2016**, *116*, 4558–4596.
- J. C. Blancon, J. Even, C. C. Stoumpos, M. G. Kanatzidis, A. D. Mohite, *Nat. Nanotechnol.* **2020**, *15*, 969–985.
- S. Zhang, S. M. Hosseini, R. Gunder, A. Petsiuk, P. Caprioglio, C. M. Wolff, S. Shoaee, P. Meredith, S. Schorr, T. Unold, P. L. Burn, D. Neher, M. Stollerfoht, *Adv. Mater.* **2019**, *31*, 1901090.
- Y. Liu, S. Akin, L. Pan, R. Uchida, N. Arora, J. V. Milić, A. Hinderhofer, F. Schreiber, A. R. Uhl, S. M. Zakeeruddin, A. Hagfeldt, M. I. Dar, M. Grätzel, *Sci. Adv.* **2019**, *5*, eaaw2543.
- G. Yang, Z. Ren, K. Liu, M. Qin, W. Deng, H. Zhang, H. Wang, J. Liang, F. Ye, Q. Liang, H. Yin, Y. Chen, Y. Zhuang, S. Li, B. Gao, J. Wang, T. Shi, X. Wang, X. Lu, H. Wu, J. Hou, D. Lei, S. K. So, Y. Yang, G. Fang, G. Li, *Nat. Photon.* **2021**, *15*, 681–689.
- H. Tsai, W. Nie, J. C. Blancon, C. C. Stoumpos, R. Asadpour, B. Harutyunyan, A. J. Neukirch, R. Verduzco, J. J. Crochet, S. Tretiak, L. Pedesseau, J. Even, M. A. Alam, G. Gupta, J. Lou, P. M. Ajayan, M. J. Bedzyk, M. G. Kanatzidis, A. D. Mohite, *Nature* **2016**, *536*, 312–316.
- S. Chen, N. Shen, L. Z. Zhang, W. G. Kong, L. H. Zhang, C. Cheng, B. M. Xu, *J. Mater. Chem. A* **2019**, *7*, 9542–9549.
- G. B. Wu, X. Li, J. Y. Zhou, J. Q. Zhang, X. N. Zhang, X. Y. Leng, P. J. Wang, M. Chen, D. Y. Zhang, K. Zhao, S. Z. Liu, H. Q. Zhou, Y. Zhang, *Adv. Mater.* **2019**, *31*, 1903889.
- J. A'vila, C. Momblona, P. P. Boix, M. Sessolo, H. J. Bolink, *Joule* **2017**, *1*, 431–442.
- M. Liu, M. B. Johnston, H. J. Snaith, *Nature* **2013**, *501*, 395.
- F. Palazon, D. Pérez-del-Re, B. Dänekamp, C. Dreessen, M. Sessolo, P. P. Boix, H. J. Bolink, *Adv. Mater.* **2019**, *31*, 1902692.
- J. Feng, Y. Jiao, H. Wang, X. Zhu, Y. Sun, M. Du, Y. Cao, D. Yang, S. Liu, *Energy Environ. Sci.* **2021**, *14*, 3035–3045.
- D. Lin, T. Zhang, J. Wang, M. Long, F. Xie, J. Chen, B. Wu, T. Shi, K. Yan, W. Xie, P. Liu, J. Xu, *Nano Energy* **2019**, *59*, 619–625.
- M.-G. La-Placa, L. Gil-Escrig, D. Guo, F. Palazon, T. J. Savenije, M. Sessolo, H. J. Bolink, *ACS Energy Lett.* **2019**, *4*, 2893–2901.
- A. Z. Chen, M. Shiu, X. Y. Deng, M. Mahmoud, D. P. Zhang, B. J. Foley, S. H. Lee, G. Giri, J. J. Choi, *Chem. Mater.* **2019**, *31*, 1336–1343.
- M. Tolan, X-ray Scattering from Soft-Matter Thin Films, Vol. 148, Springer Tracts in Modern Physics, Springer, Berlin, Germany **1999**.



## ARTICLE

## Journal Name

- 33 J. Jeong, M. Kim, J. Seo, H. Lu, P. Ahlawat, A. Mishra, Y. Yang, M. A. Hope, F. T. Eickemeyer, M. Kim, Y. J. Yoon, et al. *Nature*, **2021**, 592, 381–385.
- 34 F. Li, J. Zhang, S. Jo, M. Qin, Z. Li, T. Liu, X. Lu, Z. Zhu, A. K. Y. Jen, *Small Methods* **2019**, 8, 1900831.
- 35 Z. Chen, M. Liu, Z. Li, T. Shi, Y. Yang, H.-L. Yip, Y. Cao, *iScience* **2018**, 9, 337–346.
- 36 J. Zhang, L. Zhang, X. Li, X. Zhu, J. Yu, K. Fan, *ACS Sustain. Chem. Eng.* **2019**, 7, 3487–3495.
- 37 M. Shibata, Y. Sakai, D. Yokoyama, *J. Mater. Chem. C* **2015**, 3, 11178–11191.
- 38 A. Z. Chen, M. Shiu, J. H. Ma, M. R. Alpert, D. Zhang, B. J. Foley, D. M. Smilgies, S. H. Lee, J. J. Choi, *Nat. Commun.* **2018**, 9, 1336.
- 39 M.-C. Kim, B. J. Kim, D.-Y. Son, N.-G. Park, H. S. Jung, M. Choi, *Nano Lett.* **2016**, 16, 5756–5763.
- 40 J.-S. Yeo, R. Kang, S. Lee, Y.-J. Jeon, N. Myoung, C.-L. Lee, D.-Y. Kim, J.-M. Yun, Y.-H. Seo, S.-S. Kim, S.-I. Na, *Nano Energy* **2015**, 96–104.
- 41 H. Si, S. Zhang, S. Ma, Z. Xiong, A. Kausar, Q. Liao, Z. Zhang, A. Sattar, Z. Kang, Y. Zhang, *Adv. Energy Mater.* **2020**, 10, 1903922.
- 42 S.-M. Tatiana, S. Wiria, M.-M. Monica, *APL Materials*, **2020**, 8, 110903.
- 43 Y. Lin, Y. Bai, Y. Fang, Z. Chen, S. Yang, X. Zheng, S. Tang, Y. Liu, J. Zhao, J. Huang, *J. Phys. Chem. Lett.* **2018**, 9, 654–658.
- 44 A. A. Sutato, R. Szostak, N. Drigo, V. I. E. Queloz, P. E. Marchezi, J. C. Germino, H. C. N. Tolentino, M. K. Nazeeruddin, A. F. Nogueira, et al. *Nano Lett.* **2020**, 20, 5, 3992–3998.

View Article Online  
DOI: 10.1039/D2EE00759B